Supporting information

Enhancing Li ion transfer efficacy in PEO-based solid polymer electrolytes to promote cycling stability of Li-metal batteries

Cun Song[a], Zhengang Li[a], Jun Peng[a], Xiaohong Wu[a], Hao Peng[b], Shiyuan Zhou[a], Yu Qiao[a], Hui Sun[b], Ling Huang[a]*, Shi-Gang Sun[a]*

[a] State Key Laboratory of Physical Chemistry of Solid Surfaces, Department of Chemistry, College of Chemistry and Chemical Engineering, Xiamen University, Xiamen, 361005, P. R. China

[b] State Key Laboratory of Heavy Oil Processing, Beijing Key Laboratory of Biogas Upgrading Utilization, College of New Energy and Materials, China University of Petroleum-Beijing, Beijing, 102249, P. R. China

The ionic conductivity (κ) was calculated from the following equation:

$$\kappa = {}^{L}/_{R_b S} \tag{S1}$$

where L is the thickness of SPEs membrane, R_b is the bulk resistance of SPEs membrane that can be measured by EIS, S is the area of the stainless electrodes.

The Li^+ current fraction was calculated by the Bruce-Vincent method (Li/Li symmetrical cells with SPEs) and the ρ^+ is defined by the following equation:

$$\rho^+ = \frac{i_{ss}}{i_{\Omega}} \times \frac{\Delta V - i_{\Omega} R_{i,0} A}{\Delta V - i_{SS} R_{i,SS} A} \tag{S2}$$

where i_{ss} and i_{Ω} refer to the steady-state and initial current densities, ΔV is the dc potential across the electrolyte (10 mV in this work), $R_{i,ss}$ *and* $R_{i,0}$ refer to the interfacial resistance at steady-state and initial state, respectively, A is the area of electrode. The short-circuit test is conducted at a current density of 0.1 mA cm^{-2}, where with the battery configuration of Li/Li symmetrical cells with SPEs.

The short-circuit time prediction.[1]

In Nernst-Einstein equation theory, the ambipolar diffusion coefficient (D) can be calculated via law:

$$D = {}^{\sigma KT}/_{C_0 q^2} \tag{S3}$$

where σ (i.e., κ) is DC ionic conductivity, T is the absolute temperature, K is the Boltzmann constant, and c_0 is the Li concentration defined as the number of Li per unit volume, and q is the elementary charge.

The dendrite growth velocity v is equal to the anions drift velocity at the applied electric field. The v can be calculated by the following equation:

$$v = \mu_a E_0 \tag{S4}$$

$$E_0 = {}^{J}/_{\sigma} \tag{S5}$$

Where μ_a is the anion mobility, E_0 is the applied electric field, J is the applied current density. The time required for dendrites to grow, propagate and traverse the distance L between anode and cathode can be described by the following equation:

$$t_g = {}^{\sigma L}/_{\mu_a J} \tag{S6}$$

The μ_a can be obtained from the Einstein relation as:

$$\mu_a = qDt_a/kT \tag{S7}$$

The dendrite growth onset time (Sand's time) can be described as follows:

$$\tau_s = \pi D(eC_0/2Jt_a)^2 \tag{S8}$$

where τ_s is sand's time, e is the elementary charge, t_a is the anionic transference number that equals to 1-t_{Li^+}, and the t_{Li^+} is of the similar calculation equation to Li^+ current fraction. Based on the discussion above, the predicted short-circuit time t_{sc} can be obtained via a law:

$$t_{sc} = \pi D(eC_0/2Jt_a)^2 + \sigma L/\mu_a L \tag{S9}$$

The higher t_{sc} is, the longer lifetime of batteries are.

Table S1. The specific component proportions of PEO-, PEO/LLZTO-, PEO/LLZTO/FEC-, PLFS-SPEs.

Sample	PEO wt%	LiTFSI wt%	LLZTO wt%	FEC wt%	SN wt%
PEO-SPEs	73.93%	26.61%	--	--	--
PL-SPEs	60.60%	21.97%	17.43%	--	--
PLF-SPEs	56.38%	20.37%	16.21%	7.04%	--
PLFS-SPEs	45.74%	16.52%	13.15%	5.72%	18.87%

Table S2. The calculation results of specific parameters.

Sample	i_{Ω}/μA	i_{ss}/μA	$R_{i,0}$/Ω	$R_{i,ss}$/Ω	**ρ^+**	**κ(25℃) /10^{-4} S cm^{-1}**	$\kappa\rho^+$ /10^{-6} S cm^{-1}	**$\kappa\rho^+/\kappa\rho^+_{(PEO)}$**
PEO	9.67	2.55	603	697	**0.134**	**0.11**	1.49	**1**
PL	7.77	1.86	430	432	**0.173**	**0.09**	1.58	**1.06**
PLF	5.02	1.51	725	587	**0.201**	**0.99**	20.67	**13.85**
PLFS	16.45	8.96	279	271	**0.389**	**1.58**	61.63	**41.29**

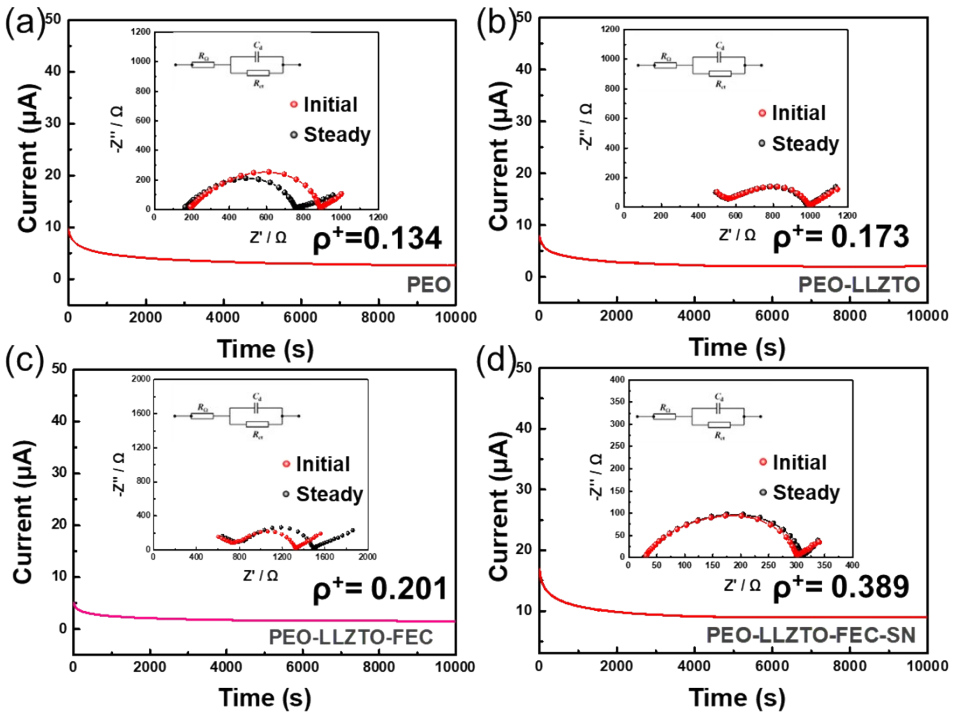

Figure S1. Li^+ current fraction (ρ^+), calculated by formula (2), of various SPEs: a, b, c, d) PEO-, PEO-LLZTO-, PEO-LLZTO-FEC-, PLFS-SPEs at 25℃.

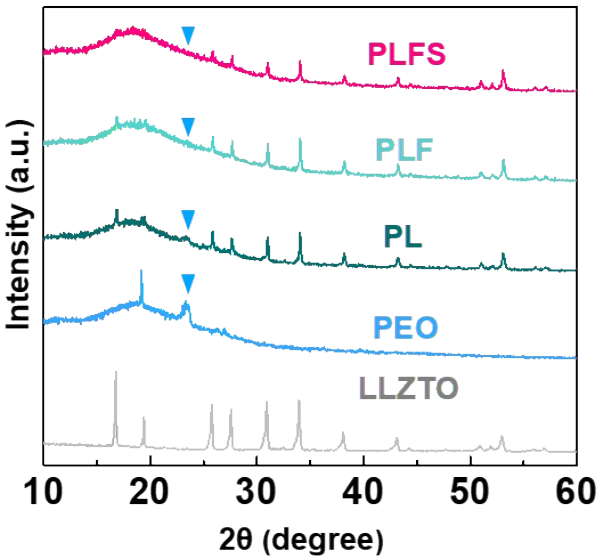

Figure S2. XRD patterns of various SPEs.

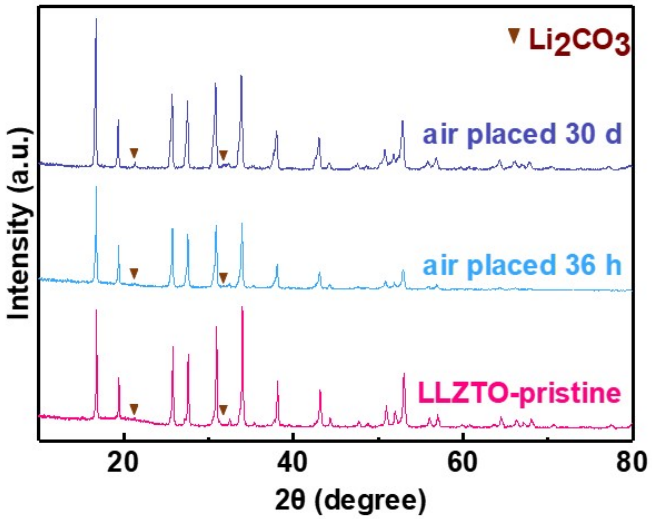

Figure S3. XRD patterns of LLZTO-pristine and air-placed for different time.

After placing LLZTO in air-exposed condition, new diffraction peak at 21.34° and 31.78° corresponding to Li_2CO_3 appeared, indicating that the Li_2CO_3 is easily formed during LLZTO synthesis and transfer process.[2]

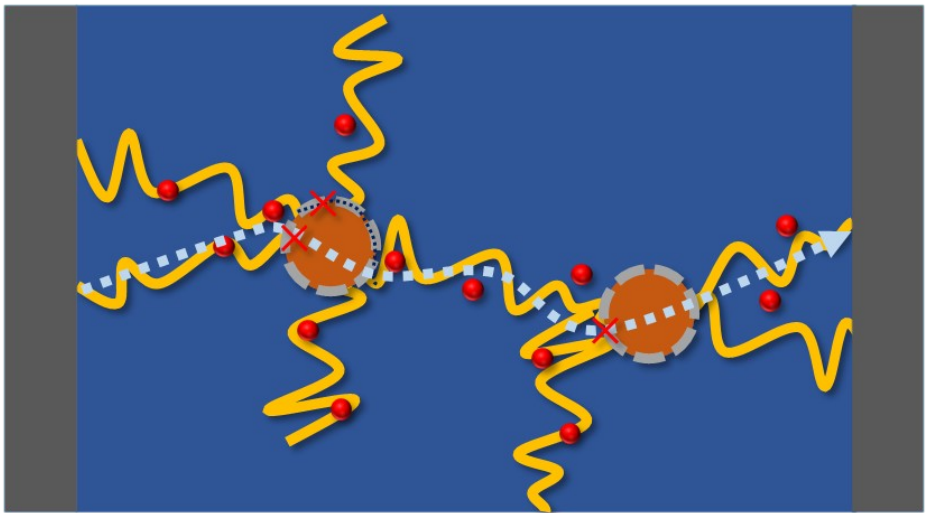

Figure S4. A possible scheme of Li^+ transfer in PEO/LLZTO electrolyte.

The incorporated LLZTO in PEO segment chains is beneficial to promote the Li^+ conduction at the LLZTO/PEO interface, while the Li_2CO_3 formed at LLZTO surface hindered this process, resulting in the decrease of ionic conductivity of PL-SPEs even though the crystallinity of PEO was decreased.

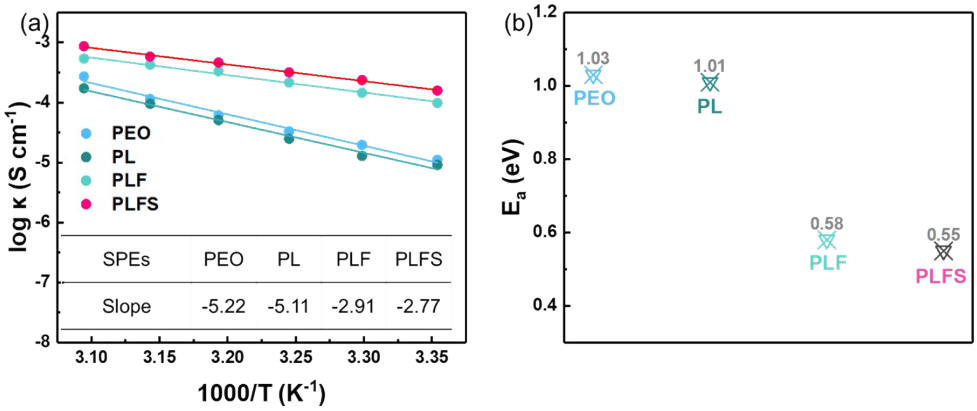

Figure S5. a) The fitting curves of Arrhenius equation of varies SPEs, b) the Li^+ transfer activation energy of varies SPEs.

The Li^+ transfer activation energy can be calculated by fitting Arrhenius equation:

$$log\ \kappa = log\ A + \frac{-E_a}{2303R}(\frac{1000}{T}) \quad \text{(S10)}$$

Where A is a constant that is proportional to the charge carrier number, E_a is the Li^+ transfer activation energy, R is the perfect gas constant.

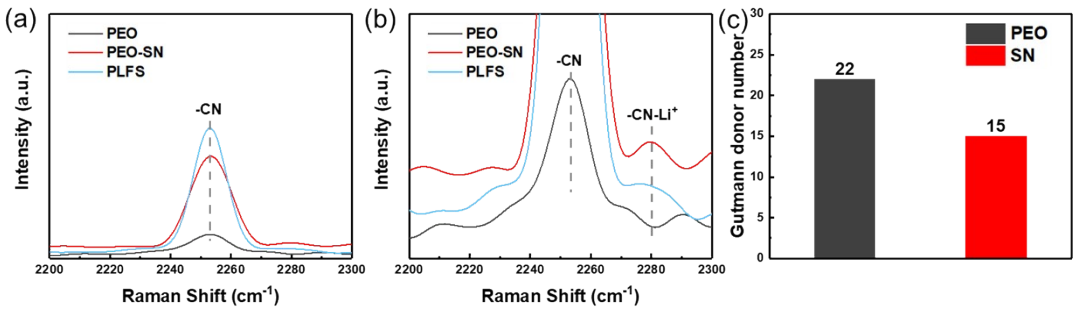

Figure S6. a, b) Raman spectra of PEO, PEO-SN and PLFS. c) Gutmann donor number of PEO and SN.

As shown in Figure S6a and S6b, a strong Raman band at 2253 cm^{-1} corresponds to the -C≡N stretching of SN. A weak signal of 2253 cm^{-1} of PEO curve originates from the residual AN solvent molecule. With the addition of SN, a Raman band at 2280 cm^{-1} corresponding to Li^+-SN appears, indicating that the SN participated in Li^+ coordination.

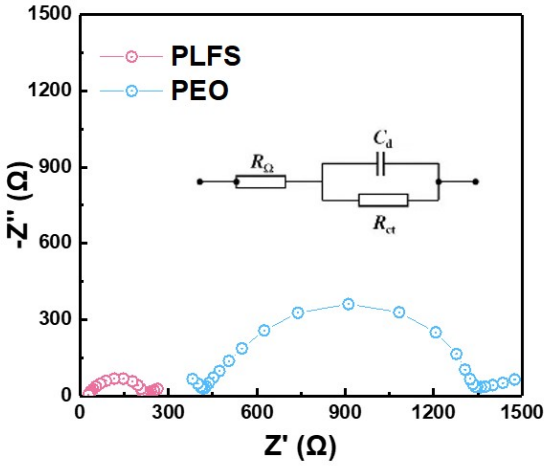

Figure S7. The impedance spectra of Li/Li symmetrical batteries with PEO- and PLFS-SPEs.

Table S3. The values of ΔH_m from DSC test and X_c of PEO- and PLFS-SPEs.

Electrolyte	ΔH_m (Jg^{-1})	X%
PEO	123.4	60.8
PLFS	36.31	17.9

The crystallinities (X_c) of SPEs can be calculated by the following equation:

$$x_c = \Delta H_m / \Delta H_{PEO} \quad \text{(S11)}$$

Where X_c represents the relative percentage of crystallinity of PEO-SPEs, and the ΔH_{PEO} represents the ΔH of 100 % crystalline PEO (203 J g^{-1}).

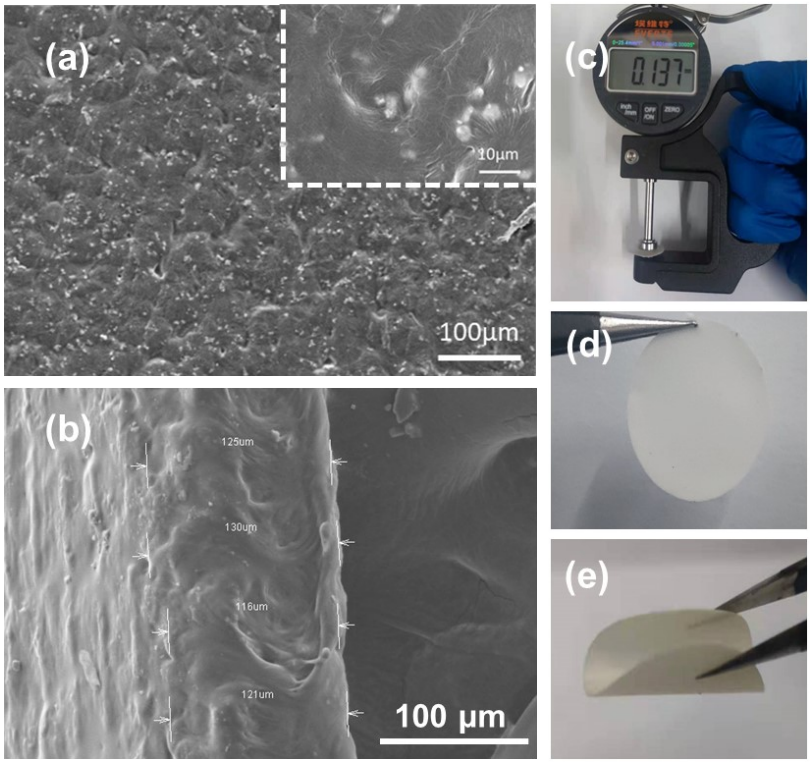

Figure S8. Morphology characterization of PLFS-SPEs. a, b) SEM images of front and side view of PLFS-SPEs' morphology. c) Thickness measurement of PLFS-SPEs. d, e) The digital picture and flexible properties of PLFS-SPEs.

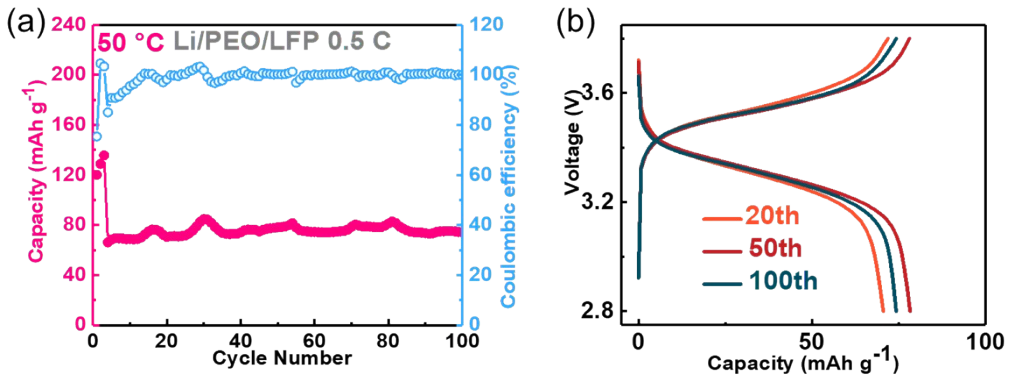

Figure S9. a, b) Cycling performance and voltage-capacity profiles of Li/PEO/LFP battery operated at 50 °C and 0.5 C.

As shown in Figure S9, when cycled at 0.1 C during the active process, the Li/PEO/LFP battery demonstrates a capacity increase to around 150 mAh g^{-1}, revealing the good contact of PEO-SPEs to electrode that have no obvious impact to capacity at low rate. When give a high rate of 0.5 C, a huge capacity discrepancy appeared, which should be attributed to the mass transfer polarization.

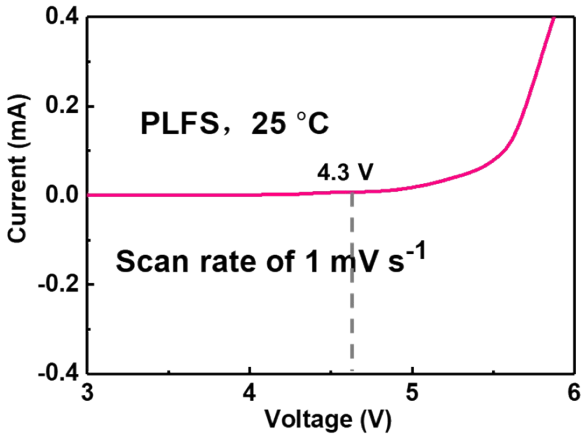

Figure S10. Linear sweep voltammetry curves of PLFS-SPEs under 25 °C at a scan rate of 1 mV s^{-1}.

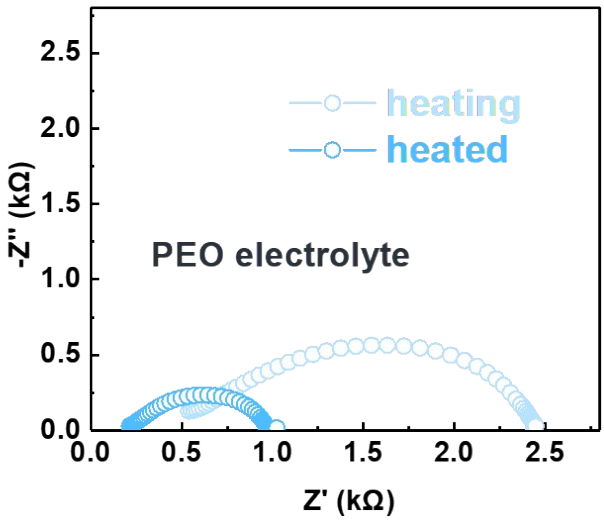

Figure S11. Comparison of interfacial resistance in Li/Li symmetry cell with PEO-SPEs before and after heat treatment.

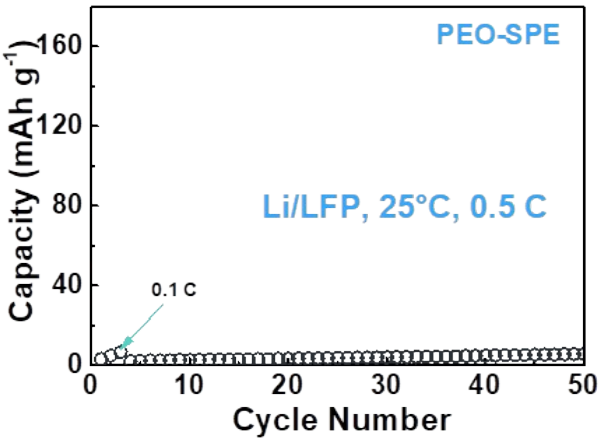

Figure S12. Electrochemical performance of Li/LFP battery assembled with PEO-SPEs at 25 °C.

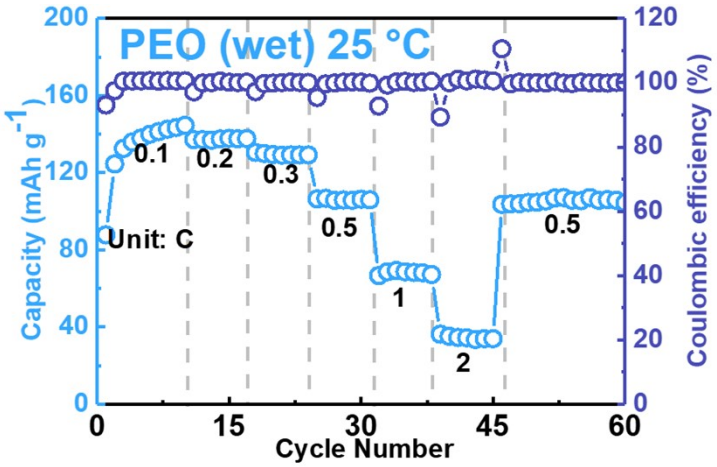

Figure S13. Rate performance of Li/LFP battery assembled with PEO-SPEs at various current density (25 ℃).

Table S4. Comparison of electrochemical performance of Li-metal batteries of this work with those reported in literatures. The Li-metal batteries were assembled with various SPEs operated at 25 °C and 50 °C.

Temperature (°C)	Cycle number	SPEs configuration	κ (10^{-4} S cm^{-1})	ρ^+	Ref.
25	700	PEO/LLZTO/FEC/SN	1.58	0.39	this work
25	30	PEO/3D LLTO	1.80	0.33	[3]
25	100	PEO-TEGDME-EMIMTFSI-LiTFSI-BP	24.0	0.32	[4]
25	120	PEO-ANP-5	3.00	0.95	[5]
50	400	PEO/LLZTO/FEC/SN	8.68	0.39	this work
60	70	PEO/LLTO/LiTFSI	2.39	---	[6]
55	100	PEO/LiTFSI+10%LLZTO	1.17	---	[7]
60	50	PEO-h-BN-LiTFSI	1.45	0.33	[8]
60	100	PEO-LLZTO-LiTFSI	0.112	0.58	[9]
55	100	70LLZO-30PEC-5(PVdF-HFP)-60LiFSI	0.52(50°C)	0.82(50°C)	[10]

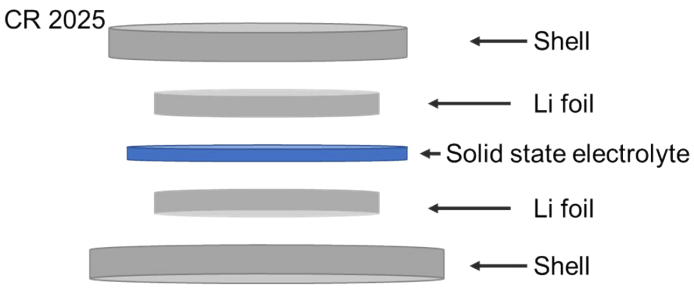

Figure S14. Diagram of Li/Li symmetric cell with CR 2025-type cell.

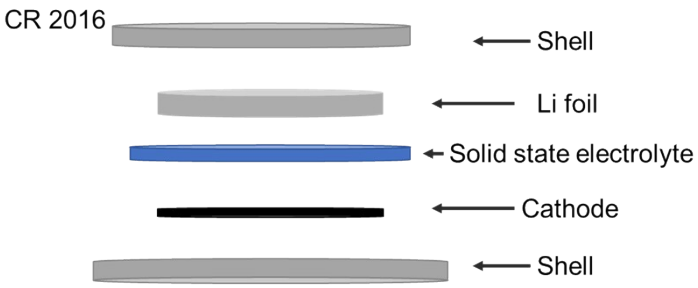

Figure S15. Diagram of Li/LFP battery with CR 2016-type cell.

References:

[1] X. Li, Y. Zheng, Q. Pan, C.Y. Li, Polymerized Ionic Liquid-Containing Interpenetrating Network Solid Polymer Electrolytes for All-Solid-State Lithium Metal Batteries. ACS Appl. Mater. Interfaces 2019, 11 (38), 34904-34912.

[2] W. Xia, B. Xu, H. Duan, X. Tang, Y. Guo, H. Kang, H. Li, H. Liu, Reaction mechanisms of lithium garnet pellets in ambient air: The effect of humidity and CO2. Journal of the American Ceramic Society 2017, 100 (7), 2832-2839.

[3] X. Wang, Y. Zhang, X. Zhang, T. Liu, Y.H. Lin, L. Li, Y. Shen, C.W. Nan, Lithium-Salt-Rich PEO/Li0.3La0.557TiO3 Interpenetrating Composite Electrolyte with Three-Dimensional Ceramic Nano-Backbone for All-Solid-State Lithium-Ion Batteries. ACS Appl. Mater. Interfaces 2018, 10 (29), 24791-24798.

[4] R. Rojaee, S. Cavallo, S. Mogurampelly, B.K. Wheatle, V. Yurkiv, R. Deivanayagam, T. Foroozan, M.G. Rasul, S. Sharifi-Asl, A.H. Phakatkar, M. Cheng, S.B. Son, Y. Pan, F. Mashayek, V. Ganesan, R. Shahbazian-Yassar, Highly-Cyclable Room-Temperature Phosphorene Polymer Electrolyte Composites for Li Metal Batteries. Adv. Funct. Mater. 2020, 30 (32), 1910749.

[5] D.M. Shin, J.E. Bachman, M.K. Taylor, J. Kamcev, J.G. Park, M.E. Ziebel, E. Velasquez, N.N. Jarenwattananon, G.K. Sethi, Y. Cui, J.R. Long, A Single-Ion Conducting Borate Network Polymer as a Viable Quasi-Solid Electrolyte for Lithium Metal Batteries. Adv. Mater. 2020, 32 (10), 1905771.

[6] Z. Wan, D. Lei, W. Yang, C. Liu, K. Shi, X. Hao, L. Shen, W. Lv, B. Li, Q.-H. Yang, F. Kang, Y.-B. He, Low Resistance-Integrated All-Solid-State Battery Achieved by Li7La3Zr2O12 Nanowire Upgrading Polyethylene Oxide (PEO) Composite Electrolyte and PEO Cathode Binder. Adv. Funct. Mater. 2019, 29 (1), 1805301.

[7] L. Chen, Y. Li, S.-P. Li, L.-Z. Fan, C.-W. Nan, J.B. Goodenough, PEO/garnet composite electrolytes for solid-state lithium batteries: From “ceramic-in-polymer” to “polymer-in-ceramic”. Nano Energy 2018, 46, 176-184.

[8] Y. Li, L. Zhang, Z. Sun, G. Gao, S. Lu, M. Zhu, Y. Zhang, Z. Jia, C. Xiao, H. Bu, K. Xi, S. Ding, Hexagonal boron nitride induces anion trapping in a polyethylene oxide based solid polymer electrolyte for lithium dendrite inhibition. J. Mater. Chem. A 2020, 8 (19), 9579-9589.

[9] C.Z. Zhao, X.Q. Zhang, X.B. Cheng, R. Zhang, R. Xu, P.Y. Chen, H.J. Peng, J.Q. Huang, Q. Zhang, An anion-immobilized composite electrolyte for dendrite-free lithium metal anodes. Proc. Natl. Acad. Sci. U.S.A. 2017, 114 (42), 11069-11074.

[10] Z. He, L. Chen, B. Zhang, Y. Liu, L.-Z. Fan, Flexible poly(ethylene carbonate)/garnet composite solid electrolyte reinforced by poly(vinylidene fluoride-hexafluoropropylene) for lithium metal batteries. J. Power Sources 2018, 392, 232-238.